Cement and Concrete Research 40 (2010) 1248–1254

Contents lists available at ScienceDirect

Cement and Concrete Research

journal homepage: http://ees.elsevier.com/CEMCON/default.asp

Synthesis and characterization of the LDH hydrotalcite–pyroaurite solid-solution series

K. Rozov [a,c,*], U. Berner [a], C. Taviot-Gueho [b], F. Leroux [b], G. Renaudin [b], D. Kulik [a], L.W. Diamond [c]

[a] Waste Management Laboratory, Paul Scherrer Institute, 5210 Villigen, Switzerland
[b] Laboratoire de Matériaux Inorganiques, CNRS UMR 6002, Université Blaise Pascal, F-63177 Aubière Cedex, France
[c] Rock-Water Interaction Group, Institute of Geological Sciences, University of Bern, Baltzerstrasse 3, CH-3012, Switzerland

ARTICLE INFO

Article history:
Received 5 June 2009
Accepted 25 August 2009

Keywords:
Hydrotalcite
(B) Characterization
Thermodynamic Calculations
(E) Waste Management
Modeling

ABSTRACT

A layered double hydroxide (LDH) hydrotalcite–pyroaurite solid-solution series $Mg_3(Al_xFe_{1-x})(CO_3)_{0.5}(OH)_8$ with $1-x=0.0, 0.1.....1.0$ was prepared by co-precipitation at 23 ± 2 °C and pH = 11.40 ± 0.03. The compositions of the solids and the reaction solutions were determined using ICP-OES (Mg, Al, Fe, and Na) and TGA techniques (CO_3^{2-}, OH^-, and H_2O). Powder X-ray diffraction was employed for phase identification and determination of the unit cell parameters a_o and c_o from peak profile analysis. The parameter $a_o = b_o$ was found to be a linear function of the composition. This dependency confirms Vegard's law and indicates the presence of a continuous solid-solution series in the hydrotalcite–pyroaurite system. TGA data show that the temperatures at which interlayer H_2O molecules and CO_3^{2-} anions are lost, and at which dehydroxylation of the layers occurs, all decrease with increasing mole fraction of iron within the hydroxide layers.
Features of the Raman spectra also depend on the iron content. The absence of Raman bands for Fe-rich members ($x_{Fe}>0.5$) is attributed to possible fluorescence phenomena.
Based on chemical analysis of both the solids and the reaction solutions after synthesis, preliminary Gibbs free energies of formation have been estimated. Values of $\Delta G°_f$(hydrotalcite) = -3773.3 ± 51.4 kJ/mol and $\Delta G°_f$(pyroaurite) = -3294.5 ± 95.8 kJ/mol were found at 296.15 K. The formal uncertainties of these formations constants are very high. Derivation of more precise values would require carefully designed solubility experiments and improved analytical techniques.

1. Introduction

The naturally occurring hydrotalcite–pyroaurite minerals $Mg_3(Al,Fe)(OH)_8(CO_3)_{0.5}\ nH_2O$ belong to the layered double hydroxide (LDH) family, which is also known as the "anionic clays". The hydroxide layers have a brucite-like crystal structure with a permanent positive charge due to the presence of trivalent Al^{3+} (Fe^{3+}) ions. This charge is compensated by anions – carbonate anions in the present case – located in the interlayer space along with water molecules. LDH solid solutions are common secondary phases in the contact zone between clays and cementitious materials, a situation which may arise in the engineered barrier system of nuclear waste disposal sites. There is growing evidence that LDH phases may play an important role in the retention of hazardous cations and especially anions (I^-, SeO_4^{2-}, SeO_3^{2-} TcO_4^{2-}, etc.) [1]. We believe that LDH phases can be treated as solid solutions, with substitution in divalent and trivalent cationic positions within the hydroxide layer and, possibly, anion exchange in the interlayer space. However, the understanding of retention properties of LDH phases is presently hampered by: 1) scarce information on thermodynamic and mixing properties of LDH solid solutions, and 2) lack of detailed knowledge of the atomic-scale uptake mechanisms for cationic and anionic contaminants.

The aim of the present work was to carry out a careful synthesis and characterization of the binary hydrotalcite–pyroaurite series $Mg_3Al(OH)_8(CO_3)_{0.5}\ nH_2O$–$Mg_3Fe(OH)_8(CO_3)_{0.5}\ nH_2O$ with varying mole fractions of Fe (0.0, 0.1.....1.0). Using various experimental techniques (X-ray power diffraction, Raman scattering spectroscopy, and thermogravimetric analysis), the primary objective was to ascertain the presence of a continuous solid-solution series in this system. The second objective was to quantify the Gibbs free energy of formation and to improve the chemical thermodynamic database [5] with the help of a thermodynamic model, based on the chemical analysis of solid and liquid phases at equilibrium.

2. Materials and methods

2.1. LDH synthesis

Samples of hydrotalcite–pyroaurite series with varying mole fraction of iron (0.0; 0.1; 0.2; 0.3; 0.4; 0.5; 0.6; 0.7; 0.8 0.9; and 1.0)

* Corresponding author. Waste Management Laboratory, Paul Scherrer Institute, 5210 Villigen, Switzerland.
E-mail address: urs.berner@psi.ch (K. Rozov).

0008-8846/$ – see front matter © 2009 Elsevier Ltd. All rights reserved.
doi:10.1016/j.cemconres.2009.08.031

have been prepared by a co-precipitation method according to [2] at 23 ± 2 °C and pH = 11.40 ± 0.03.

The syntheses were performed under N_2 gas flow by slow addition (at a rate of 0.04 mL/min) of 60 mL 0.1 M metal-nitrate solution with $Mg/(Al+Fe) = 3.0 \pm 0.1$ into a reactor containing 300 mL of stirred 0.025 M Na_2CO_3 solution (Fig. 1). In order to produce increased amounts of solid, a second set of syntheses was performed using a six-fold amount of the solutions in a 2000 mL reactor. To avoid precipitation of iron hydroxides, sufficient amounts of concentrated HNO_3 had previously been added to the Fe-containing nitrate stock solutions. To maintain pH ≈ 11.40, a 2 M NaOH solution was added simultaneously (at a maximum rate of 0.05 mL/min) into the reactor using an automated titrator "Titroprocessor 670" (Metrohm AG). All stock solutions were prepared using Merck® "pro analysis" chemicals and MilliQ water generated by the "Millipore" water purification system. The overall reaction can be described as:

$$3Mg(NO_3)_2 + xAl(NO_3)_3 + (1-x)Fe(NO_3)_3 + 8NaOH + 0.5Na_2CO_3 \rightarrow Mg_3[Al_xFe_{1-x}](OH)_8(CO_3)_{0.5} \cdot nH_2O + 9NaNO_3 \quad (1)$$

After the addition step, the suspension was aged for 24 h in the stirred reactor under controlled pH (pH = 11.40 ± 0.03). It was then separated from the mother solution by centrifuging at 95,000 *g* for 1 h. About 40 mL of MilliQ water was used to wash about 500 mg of the precipitate and the mixture was then shaken and centrifuged again at 95,000 *g* for 10 min. This washing procedure was repeated 3 times until the electrical conductivity of the supernatant was below 12 µS, which means that the concentration of $NaNO_3$ (provided that sodium nitrate is the only solute) in these solutions is below 7.2 10^{-5} mol/L. This in turn means that $NaNO_3$ impurities in the solid phase were below 0.05 wt.%. The washed solids were finally dried in an oven at 60 °C for 24 h.

2.2. Analyses and characterization

2.2.1. ICP-OES analyses

The contents of Mg, Al, Fe and Na in the solid and liquid phases were determined by ICP-OES using a Perkin-Elmer (type Vista Pro) instrument. The synthesis solutions were analyzed after acidifying with some drops of concentrated nitric acid (dilution was recorded by a balance). The solids were analyzed after dissolving 20 mg of solid in 60 g of 0.5 M HNO_3. Internal standards were prepared from ICP quality (Merck®) multi-element standard solutions of Mg, Al, Fe and Na.

2.2.2. Ion chromatography

Nitrate anions in the product liquid phase were analyzed spectrophotometrically after separation by ion chromatography (Dionex DX-600 Ion Chromatograph with IonPac AS16/AG16 chromatographic columns). Solutions of KNO_3 (Merck®) were used for the preparation of the internal standards.

2.2.3. Total inorganic carbon analysis (TIC)

A Shimadzu TOC-V analyzer was used to determine the carbonate content in the liquid phase. Internal standard solutions were prepared using Na_2CO_3 (Merck®) and degassed MilliQ water.

2.2.4. Powder X-ray diffraction (PXRD)

The powder X-ray diffraction (PXRD) technique was applied to characterize the precipitated solids using a Phillips XPert-Pro diffractometer. No internal standards for possible specimen displacement were used. The diagrams were recorded with CuKα radiation at ambient temperature within a 2θ-range from 5° to 70°, using a step size of 0.0168° and a counting time of 20 min.

The cell parameters were determined from peak profile analysis using the program "FullProf" (full pattern matching — pseudo–Voigt profile function) [3].

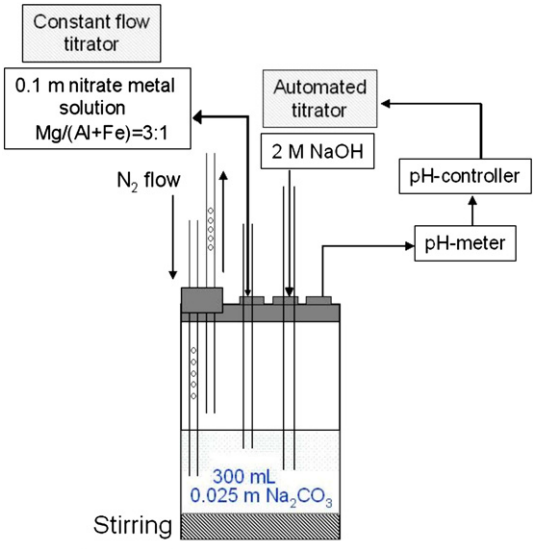

Fig. 1. Experimental setup for the co-precipitation synthesis of hydrotalcite–pyroaurite solids.

The cell parameters were also determined from the Bragg equation, using the relationship between interlayer distances (d_{hkl}), the h,k,l indexes, and the lattice parameters for hexagonal symmetry based only the first 4 reflections. The results of both methods are represented in Figs. 4 and 5.

2.2.5. Thermogravimetric analyses (TGA)

TGA was carried out in order to determine the contents of interlayer water, and of hydroxide and carbonate anions in the solids. Measurements were performed on a Mettler Toledo TGA instrument. Before the measurements the samples were dried at 60 °C for 15 min. The weight loss of the solids in air was analyzed from 60 °C to 1000 °C with a heating rate of 5 °C/min.

2.2.6. Raman spectroscopy

Raman scattering spectra were acquired using a Jobin Yvon Horiba LabRam HR 800 spectrometer equipped with an Olympus BX41 petrographic microscope and a 532.12 nm (green) frequency-doubled Nd:YAG laser. The spectra were calibrated using silicon and Ne standards. Before measuring, the samples were dried at 60 °C for 6 h. The spectra were manipulated and recorded using the LabSpec™ v. 4.14 software. The band component analysis was carried out using the "PeakFit" software package, and the band fitting and smoothing were done using Gaussian functions. The spectra were recorded from 250 to 3800 cm^{-1}.

2.2.7. Determination of solid compositions

In order to calculate the compositional formulae of the solids we combined the ICP-OES analyses of Mg, Al, Fe and Na with the TGA measurements: we assumed that the solid products after the TGA analysis (at 1000 °C) are composed of mixtures of MgO, Al_2O_3 and Fe_2O_3 and that the removal of interlayer water, hydroxyl and carbonate groups can be described as follows:

$$Mg_3(Al_xFe_{1-x})(CO_3)_{0.5}(OH)_8 \cdot nH_2O \rightarrow Mg_3(Al_xFe_{1-x})(CO_3)_{0.5}(OH)_8 + nH_2O \quad (2)$$

$$Mg_3(Al_xFe_{1-x})(CO_3)_{0.5}(OH)_8 \rightarrow Mg_3(Al_xFe_{1-x})(CO_3)_{0.5}O_4 + 4H_2O \quad (3)$$

$$Mg_3(Al_xFe_{1-x})(CO_3)_{0.5}O_4 \rightarrow Mg_3(Al_xFe_{1-x})O_{4.5} + 0.5CO_2 \quad (4)$$

The stoichiometric coefficients given in Table 1 can be derived using the Mg/(Al + Fe) ratio determined by ICP-OES, the amount of

Table 1
Stoichiometric formulae, estimated standard Gibbs free energies and total solubility products of the synthesized solids.

Mole fraction of iron in solids. (x_{Fe})	Stoichiometric formulae[a] (including analytical errors)	$Mg^{II}/(Al^{III}+Fe^{III})$ in solid phase	$G°_f$ kJ/mol (without interlayer water)	logKsp
0	$Mg_3Al_{1.019\,(0.102)}(CO_3)_{0.472\,(0.031)}(OH)_{8.114\,(0.243)}\cdot 2.53H_2O$	2.94 ± 0.29	-3773.43 ± 124.15	-68.92 ± 3.50
0	$Mg_3Al_{1.021\,(0.099)}(CO_3)_{0.666\,(0.019)}(OH)_{7.730\,(0.258)}\cdot 2.46H_2O$	2.94 ± 0.29	-3818.71 ± 118.97	-69.52 ± 3.54
0.098 ± 0.007	$Mg_3Al_{0.896\,(0.083)}Fe_{0.097\,(0.019)}(CO_3)0.336_{(0.017)}(OH)_{8.305\,(0.271)}\cdot 2.51H_2O$	3.02 ± 0.27	-3671.87 ± 112.49	-68.76 ± 3.55
0.192 ± 0.012	$Mg_3Al_{0.827\,(0.080)}Fe0.192_{(0.020)}(CO_3)_{0.536\,(0.017)}(OH)7.987_{(0.267)}\cdot 2.62H_2O$	2.94 ± 0.24	-3690.29 ± 112.49	-67.79 ± 3.62
0.203 ± 0.013	$Mg_3Al_{0.802\,(0.080)}Fe_{0.205\,(0.020)}(CO_3)_{0.537\,(0.017)}(OH)_{7.946\,(0.267)}\cdot 2.67H_2O$	2.98 ± 0.24	-3701.77 ± 111.44	-71.61 ± 3.75
0.304 ± 0.019	$Mg_3Al_{0.695\,(0.069)}Fe_{0.304\,(0.030)}(CO_3)_{0.481\,(0.016)}(OH)8.034_{(0.267)}\cdot 2.52H_2O$	3.00 ± 0.23	-3623.89 ± 104.99	-70.83 ± 3.61
0.391 ± 0.024	$Mg_3Al_{0.625\,(0.062)}Fe0.394_{(0.039)}(CO3)0.553_{(0.019)}(OH)_{7.951\,(0.267)}\cdot 2.50H_2O$	2.94 ± 0.21	-3604.44 ± 103.58	-68.7 ± 3.65
0.497 ± 0.030	$Mg_3Al0.502_{(0.050)}Fe0.496_{(0.050)}(CO3)0.361_{(0.013)}(OH)_{8.276\,(0.278)}\cdot 2.45H_2O$	3.01 ± 0.21	-3499.21 ± 95.95	-69.25 ± 3.63
0.603 ± 0.037	$Mg_3Al_{0.415\,(0.041)}Fe_{0.619\,(0.062)}(CO_3)0.531_{(0.020)}(OH)_{8.039\,(0.270)}\cdot 2.47H_2O$	2.90 ± 0.21	-3513.97 ± 95.17	-69.51 ± 3.74
0.701 ± 0.044	$Mg_3Al0.299_{(0.030)}Fe0.703_{(0.070)}(CO_3)0.248_{(0.009)}(OH)8.509_{(0.281)}\cdot 2.55H_2O$	2.99 ± 0.23	-3387.14 ± 85.67	-70.09 ± 3.68
0.805 ± 0.052	$Mg_3Al_{0.207\,(0.021)}Fe_{0.839\,(0.084)}(CO_3)_{0.491\,(0.019)}(OH)_{8.157\,(0.275)}\cdot 2.55H_2O$	2.87 ± 0.24	-3418.14 ± 86.37	-70.23 ± 3.81
0.897 ± 0.060	$Mg_3Al_{0.108\,(0.005)}Fe_{0.902\,(0.090)}(CO_3)_{0.342\,(0.013)}(OH)_{8.344\,(0.260)}\cdot 2.64H_2O$	2.97 ± 0.27	-3323.14 ± 71.95	-70.38 ± 3.53
1	$Mg_3Fe_{1.086\,(0.108)}(CO_3)_{0.343\,(0.014)}(OH)_{8.570\,(0.296)}\cdot 2.15H_2O$	2.76 ± 0.28	-3321.52 ± 78.70	-72.36 ± 3.99

[a] Calculated mole numbers of components are given to three decimal places to reach electrical neutrality. The real certainty of the analyses is lower, as indicated by numbers in brackets, e.g. (0.102) denotes ±0.102.

CO_2 and H_2O lost between 60 °C and 1000 °C, and considering the electroneutrality of the solid. The uncertainties are based on the assumption that the analytical error of the applied ICP-OES technique is ±5% for Mg, Al and Fe and that the error of TGA analyses is well below 1%. Note that the analysis of Na in all samples was less than 0.015 ± 0.005 wt.%, which is a very strong indication that Na-containing phases (i.e., $NaNO_3$) are absent after the washing and drying procedure (see above).

2.2.8. Estimation of Gibbs free energies

Standard Gibbs free energies of formation of the solids were estimated according to the following scheme: 1) the speciation of the synthesis solutions was modelled in order to obtain the activities and chemical potentials of relevant solutes (i.e., Mg^{2+}, Al^{3+}, Fe^{3+}, OH^-, and CO_3^{2-}). To perform these calculations we used the Gibbs free energy minimization software GEMS [4], including the thermodynamic data given in [5]. From the chemical potential of the solutes and from the stoichiometric coefficients in Table 1, the Gibbs free energies were obtained according to:

$$G_f^\circ(\mathrm{Htlc-Pyr}) = a\mu(Mg^{2+}) + b\mu(Al^{3+}) + c\mu(Fe^{3+}) + d\mu(OH^-) + e\mu(CO_3^{2-}), \quad (5)$$

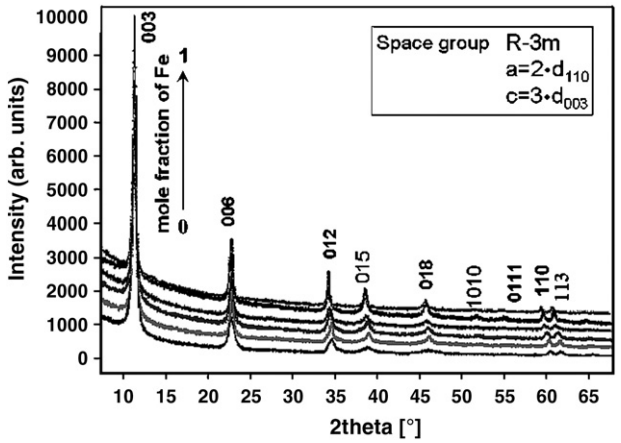

Fig. 2. X-ray diffractograms of synthetic hydrotalcite–pyroaurite solid-solution series with $x_{Fe}=0.0$, 0.1, 0.2, 0.3, 0.4, 0.5, 0.6, 0.7, 0.8, 0.9, and 1.0 (bottom – up).

a–e: stoichiometric coefficients; μ_i: chemical potentials, evaluated from the synthesis solution.

The total solubility products of individual solids were also calculated based on the activities of the relevant components in the "synthesis" solutions, using Eq. (6):

$$\log_{10}\mathrm{Ksp} = \log_{10}[Mg^{2+a}Al^{3+b}Fe^{3+c}OH^{-d}CO_3^{2-e}], \quad (6)$$

3. Results

All the solids display powder X-ray diffraction spectra typical of LDH materials (Fig. 2). However, the peaks are broad, presumably due to the simultaneous effects of small coherent domain size and structural disorder. This prevented us from performing Rietveld structural refinements. The diffraction peaks were indexed on a hexagonal unit cell with the space group R-3m [6,7]. The cell parameters gathered in Table 2 were obtained from profile peak analysis and from a Bragg-type evaluation. An example of the unit cell refinement is given in Fig. 3. It is also important to note that none of the spectra indicates the presence of a second phase.

The variation of the cell parameter a as a function of the iron content x (Fig. 4) is in excellent agreement with the Vegard's law [8], thereby demonstrating the existence of a continuous solid solution throughout the hydrotalcite–pyroaurite series. By linear regression it was found that $a_x=(3.0600\pm0.0004)+(0.0500\pm0.0007)\times x_{Fe}^{3+}$ (Å).

This equation can be compared to that expected for an idealized octahedral layer structure built with regular $M(OH)_6$ octahedra. In this case, the cell parameter a of the rhombohedral cell must be equal to $\sqrt{2}d_{M-OH}$, d_{M-OH} $(=R_M^{n+}+R_{OH}^-)$ being the mean M–OH distance within the hydroxide layer and $\frac{da}{dR}=\sqrt{2}$. On the other hand, one can calculate a mean ionic radius within the hydroxide layers equal to:

$$R_m = 0.75R_{Mg}^{2+} + 0.25xR_{Al}^{3+} + 0.25(1-x)R_{Fe}^{3+} \quad (7)$$

in the 3:1 hydrotalcite–pyroaurite structure and $\frac{dR_m}{dx}=0.25\cdot(R_{Al}^{3+}+R_{Fe}^{3+})$.

Table 2
Cell parameters determined from peak profile analysis and from Bragg evaluation and refined in the space group R-3m.

Approximate mole fraction of iron in solid	$a_o = b_o$, Å		c_o, Å	
	W-B	Rv	W-B	Rv
0.0	3.063 ± 0.004	3.0615 ± 0.0003	23.445 ± 0.074	23.380 ± 0.006
0.1	3.064 ± 0.001	–	23.346 ± 0.018	–
0.2	3.071 ± 0.001	3.0694 ± 0.0002	23.380 ± 0.024	23.352 ± 0.003
0.3	3.074 ± 0.001	–	23.354 ± 0.014	–
0.4	3.081 ± 0.001	3.0758 ± 0.0002	23.428 ± 0.014	23.392 ± 0.004
0.5	3.085 ± 0.001	–	23.409 ± 0.014	–
0.6	3.093 ± 0.001	3.0909 ± 0.0003	23.434 ± 0.020	23.382 ± 0.005
0.7	3.096 ± 0.001	–	23.439 ± 0.012	–
0.8	3.101 ± 0.001	3.0995 ± 0.0002	23.460 ± 0.012	23.392 ± 0.003
0.9	3.105 ± 0.001	–	23.481 ± 0.010	–
1.0	3.110 ± 0.001	3.1107 ± 0.0002	23.539 ± 0.016	23.537 ± 0.003

W-B — results obtained from the Bragg evaluation, Rv — results obtained from profile peak analysis.

Since $\frac{da}{dx} = \frac{da}{dR} \cdot \frac{dR}{dx}$ and using R^{3+}_{Al} (in octahedral coordination) = 0.535 Å, R^{3+}_{Fe} (in octahedral coordination) = 0.645 Å [9] and $Mg^{2+}/(Al^{3+} + Fe^{3+}) = 2.91 \pm 0.15$, one can calculate the slope da_o/dx:

$$\frac{da}{dx} = \sqrt{2} \cdot (0.26 \pm 0.01) \cdot (R_{Fe3+} - R_{Al3+}) = 0.042 \pm 0.002 \quad (8)$$

We observe a significant difference between the theoretical slope of 0.042 based on regular $M(OH)_6$ octahedra and the observed slope of 0.050. Such a difference can be easily explained by the fact that $M(OH)_6$ octahedra within LDH hydroxide layers are distorted, being flattened in the direction normal to the layers and extended in a plane parallel to the layers, even more than is found in brucite or gibbsite [10].

The lattice parameter *c* (Fig. 5 and Table 2, see also Section 2.2.4.) corresponds to the 3 layer rhombohedral polytype 3R (Fig.6). The resulting interlayer distance $d_{003} = c/3$ depends on the layer charge density, the nature of the interlayer anion (CO_3^{2-}) and on the number of water molecules in the interlayer space. Since the $Mg^{2+}/(Al^{3+} + Fe^{3+})$ ratio is kept constant, one can reasonably attribute the slight increase of d_{003} as a function of *x* from 7.793 to 7.845 Å to the replacement of Al^{3+} ($R^{3+}_{Al} = 0.535$ Å) by Fe^{3+}, which displays a higher ionic radius ($R^{3+}_{Fe} = 0.645$ Å) and thus longer M–OH distances. This interpretation is consistent with the chemical analysis showing a constant $Mg^{2+}/(Al^{3+} + Fe^{3+})$ ratio and no remarkable change of the composition of the interlayer space with respect to both water molecules (approx. 2.51 ± 0.13 per formula unit) and interlayer anions (Table 3).

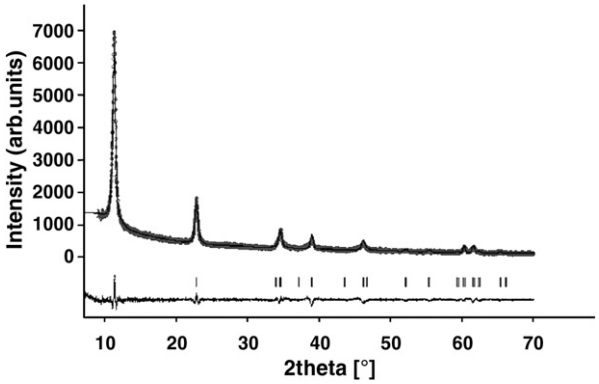

Fig. 3. Results of the profile analysis of XRD patterns for $Mg_3Al_{0.823}Fe_{0.191}(CO_3)_{0.532}(OH)_{7.978} \cdot 2.615H_2O$ ($x = 0.191$) in the space group R-3m: experimental X-ray diffraction (cross), calculated (line), Bragg reflections (ticks) and difference profiles; the refined cell parameters are $a = 3{,}0694(2)$ Å and $c = 23{,}352(3)$ Å.

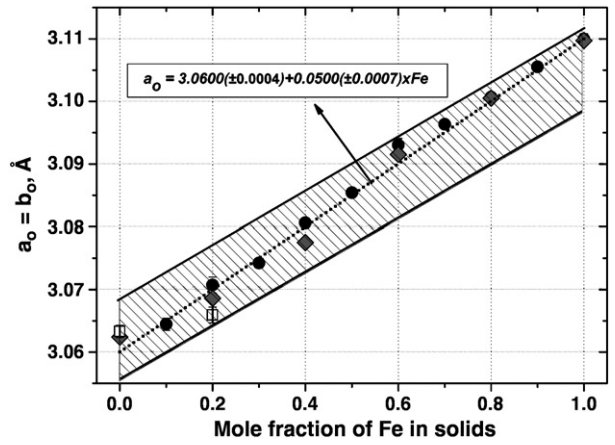

Fig. 4. Unit cell parameters (a) as a function of the mole fraction of iron. The shaded area represents the fitted slope of 0.050 and encompasses all experimental points including their uncertainties. The dashed line represents the theoretical curve based on a regular octahedral layer. Filled diamonds represent refined parameters determined from peak profile analysis and filled circles represent parameters evaluated using the Bragg-type equation. Open squares represent solids produced in a reactor vessel with increased volumes (2000 mL).

According to the literature [11–13] the thermal decomposition of LDHs includes three main stages, i.e., the loss of interlayer water, the decomposition of structural hydroxyl groups and finally the decomposition of interlayer carbonate anions.

For the present compounds, these three decomposition steps were evaluated by determining the second derivative of the TGA-curve (Fig. 7). It was observed that an increase of the mole fraction of iron causes a decrease of the temperature of dehydroxylation of brucite-like layers from 230 to 180 °C, in agreement with the fact that the short Al–OH bond distance is stronger than the longer Fe–OH bond distance. Similarly, the temperature of decarbonation decreases from 440 to 407 °C with increasing mole fraction of iron.

Raman spectroscopy is specifically suited to identify the nature of the interlayer anion and to investigate its interactions with the rest of the structure, particularly the hydrogen-bond network.

Raman bands (around 540 cm^{-1}, 1060 cm^{-1}, 1370–1390 cm^{-1} and 3400–3700 cm^{-1}) which are typical [14] for hydrotalcite structure were observed only in solids with $x_{Fe} \leq 0.5$ (see discussion below). The band around 540 cm^{-1} (Fig. 8A) originates from the interlayer carbonate-water unit, where the two hydrogen atoms of the H_2O molecule are bridged to two oxygen atoms of the carbonate anion,

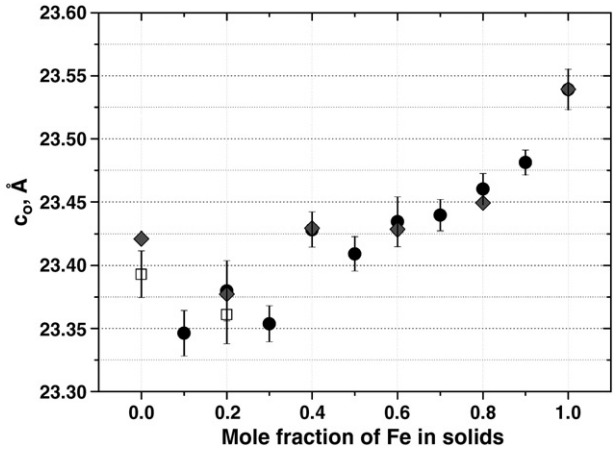

Fig. 5. Dependence of the unit cell parameter c_o on the mole fraction of Fe. Filled diamonds represent refined parameters determined from peak profile analysis and filled circles represent parameters evaluated using the Bragg-type equation. Open squares represent solids produced in a reactor vessel with increased volumes (2000 mL).

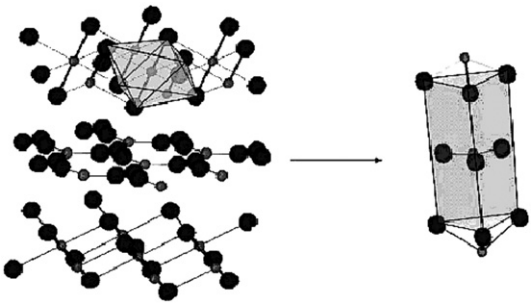

Fig. 6. Layer–interlayer configuration in R-3m space group: OH groups from adjacent octahedral layers superimpose, forming a prismatic environment around interlayer carbonate anions.

strongly indicating the presence of carbonate in the system [14]. The band around 1060 cm^{-1} (Fig. 8B) corresponds to interlayer carbonate anions (υ_1) associated with [M(II), M(III)]$(OH)_6$ structural units in the brucite-type layers. From $x = 0$ to 0.3 the position of this peak remains almost constant, indicating no change in symmetry of the CO_3^{2-} anions. The very weak band around 1370–1390 cm^{-1} (υ_4) (Fig. 8C) also belongs to the carbonate anions, either free or bound to interlayer water molecules or hydroxide groups of the brucite-like sheet. The large band around 3400–3700 cm^{-1} (Fig. 8D) represents OH-stretching vibrations from OH groups as well as interlayer water molecules.

The formation of a unique phase of LDH type throughout the whole composition range has been confirmed by PXRD analysis. Hence, the disappearance of the Raman signals above $x = 0.5$ cannot be ascribed to a structural change. It is likely due to masking by fluorescence of the iron-rich samples. Attempts to acquire spectra using a less absorbing 633 nm He–Ne (red) laser failed to improve the situation. Finally, it is worth mentioning the absence of a peak at 1080 cm^{-1}, attributed to interlayer nitrate anions [14], indicating that the washing procedure was successful and that the investigated solids are free of $NaNO_3$, in accordance with the low conductance (12 μS) measured in the washing solution and with the fact that no Na was found in the analysis of the solid phase.

Chemical compositions of the "synthesis" solutions and solids are provided in Tables 1 and 3. It should be noted that the synthesis was carried out in solutions with "high" ionic strength between 0.1 and 0.2 mol/kg. As a consequence, one measures concentrations at the mmol/kg-level for Na, NO_3^- and CO_3^{2-}. The analytical error for these concentrations is assumed to be about ±5%. The metals Mg, Al and Fe were found at concentrations between 0.1 and 22 μmol/kg. According to [15] the analytical error of the ICP-OES technique is more than ±5% when Fe lies in the range from 10^{-8} to 10^{-6} mol/kg. A further complication is that these low concentrations of Mg, Al and Fe must be determined in a matrix of high Na concentration. It was recognized,

Table 3
Composition of solutions after synthesis at 23–24 °C and pH = 11.40 ± 0.05.

Mg	Al	Fe	Na	NO_3^-	CO_3^{2-}	Approximate mole fraction of iron in solid
μmol/kg			mmol/kg			
12.0	2.67	Below dl	82.0	37.2	19.1	0.0
5.7	2.05	Below dl	78.0	35.6	20.3	0.0
8.6	4.83	0.28	120.0	74.5	18.6	0.1
21.8	8.48	1.67	132.0	76.0	18.3	0.2
1.2	2.08	Below dl	128.0	76.5	20.0	0.2
2.3	7.31	0.09	119.0	74.6	18.9	0.3
13.6	7.18	2.73	136.0	79.2	18.5	0.4
10.1	6.97	1.68	123.0	73.6	19.1	0.5
16.1	5.18	3.77	129.0	76.1	24.3	0.6
9.8	5.42	2.46	123.0	75.3	20.7	0.7
16.2	5.10	4.92	129.0	77.0	20.2	0.8
9.8	2.42	2.67	122.0	74.1	19.4	0.9
16.8	<0.001	4.68	129.0	76.8	20.0	1.0

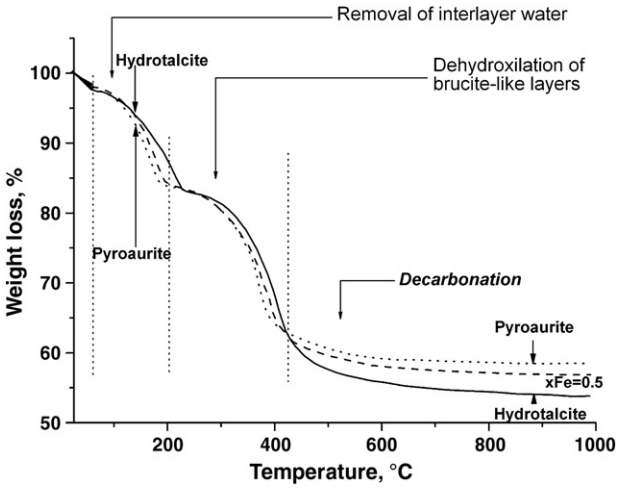

Fig. 7. TGA curves of hydrotalcite–pyroaurite samples. The applied heating rate was 5 °C/min. Samples were dried for 15 min at 60 °C before analysis.

for example, that Mg varies over the range 5.7 to 12.0 μmol/kg in two identical experiments (first two rows of Table 3). Hence, we concluded that the analytical error for Mg in the "synthesis" solution is substantially higher than 5%. From the average of Mg analyses provided in Table 3, an analytical error of at least ±50% was estimated. For Al, the measured concentrations vary in the range 2.1 to 8.5 μmol/kg but do not show a clear tendency as a function of the mole fraction of Fe, as could be expected from general chemical considerations. Hence, from the standard deviation it could be inferred that the analytical error of the Al determinations is also about ±50%. However, in the case of pyroaurite the analysis shows traces of Al in the range 0.001 μmol/kg, although Al should not be present at all in this particular "synthesis" solution. Contrary to the above statement this low detection limit indicates that the analytical error of Al is most likely less than ±50%.

In the case of iron a similar situation was observed. A clear trend of analytical results was hard to see in the sequence of Fe concentrations from hydrotalcite to pyroaurite, although the values varied from 0.09 to 4.9 μmol/kg. A simple estimate based on the standard deviation and assuming no trend in the data reveals that the analytical error could be as high as ±66%. From simultaneously performed analyses of internal standards, it was inferred that the analytical error for Fe is about 15% and for Mg the error is about 10%. However, using these latter uncertainties it turned out that the analytical errors of synthesis solution compositions do not significantly contribute to the total error of calculated standard Gibbs free energies (see below).

The determination of the stoichiometric composition of the solid phases has been outlined in Section 2.2.7. Table 1 reveals that the average Mg(II)/(Al(III) + Fe(III)) ratio is close to the desired value of 3 (2.91 ± 0.15). The analyses of water, hydroxide and carbonate are remarkably constant in the range from hydrotalcite to pyroaurite. It was found that each formula unit contains 2.51 ± 0.13 H_2O, 8.15 ± 0.24 OH^- and 0.45 ± 0.12 CO_3^{2-}. Note that, when contemplating varying compositions, the uncertainties in the values of carbonate and hydroxide anions must correspond to each other because there are no other anions available (charge balance). It has already been demonstrated above that in washed solids the impurities of $NaNO_3$ are not significant.

The solids as described in Table 1 precipitated from the solutions presented in Table 3. In this first study we neglected possible effects of oversaturation and we assumed equilibrium between the precipitated solids and their corresponding "synthesis" solutions. Based on the uncertainties of the stoichiometric coefficients many possible compositions exist which are compatible with the formulae presented in Table 1. In order to estimate the range of possible free energies, calculations were performed for the most extreme compositions

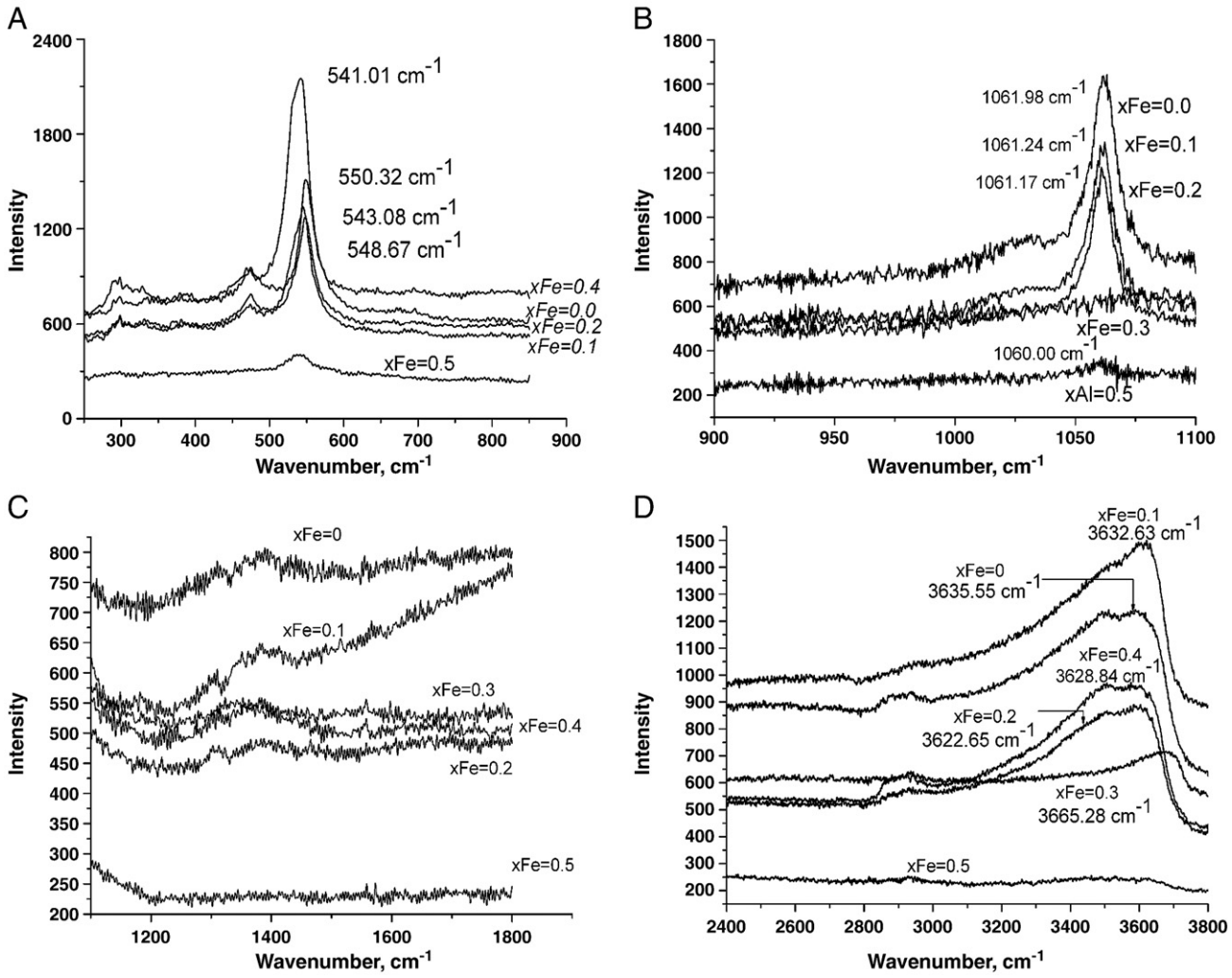

Fig. 8. Raman spectra of hydrotalcite–pyroaurite samples with low mole fraction of Fe ($x_{Fe} \leq 0.5$; left column). A more detailed description of individual spectra is given in the text.

within the analyzed range. As an example, Gibbs free energies of the solid with $x_{Fe} = 0.192$ (row 4 of Table 1) are shown:

$$Mg_3Al_{0.910}Fe_{0.211}(CO_3)_{0.553}(OH)_{8.258} \quad \Delta G_f^\circ = -3802.8 \text{kJ/mol} \tag{9}$$

$$Mg_3Al_{0.745}Fe_{0.173}(CO_3)_{0.518}(OH)_{7.717} \quad \Delta G_f^\circ = -3577.8 \text{kJ/mol} \tag{10}$$

As a result, the average of -3690.3 ± 112.5 kJ/mol was selected for the solid with $x_{Fe} = 0.192$.

Note that the interlayer water ("nH_2O", corresponding to n times 237.182 kJ/mol) is not included in the calculation of the Gibbs free energy in order to obtain results that can be compared on a common "water-free" basis. It is evident that the interlayer water is essential for stabilizing the structure of LDH, but it is also essential that comparisons within the solid-solution series are made with an identical amount of interlayer water (i.e. we have arbitrarily selected $n = 0$).

The estimated Gibbs free energies were regressed against the mole fraction of iron. The weighted linear regression produced:

$$\Delta G_f^\circ = (-3773.3 \pm 51.4) + (478.8 \pm 80.8) \cdot x_{Fe} [\text{kJ/mol}], R^2 = 0.981$$

(see Fig. 9), from which we obtained the standard Gibbs free energies of the end-members:

$$\Delta G_f^\circ(\text{hydrotalcite}) = -3773.3 \pm 51.4 \text{kJ/mol};$$

$$\Delta G_f^\circ(\text{pyroaurite}) = -3294.5 \pm 95.8 \text{kJ/mol}.$$

There is a fair agreement of ΔG°_f of hydrotalcite with the value from [16]. These authors provided -1043.1 ± 2.1 kJ/mol for a solid having the stoichiometry $Mg_{0.74}Al_{0.26}(OH)_2(CO_3)_{0.13}$ $0.39H_2O$.

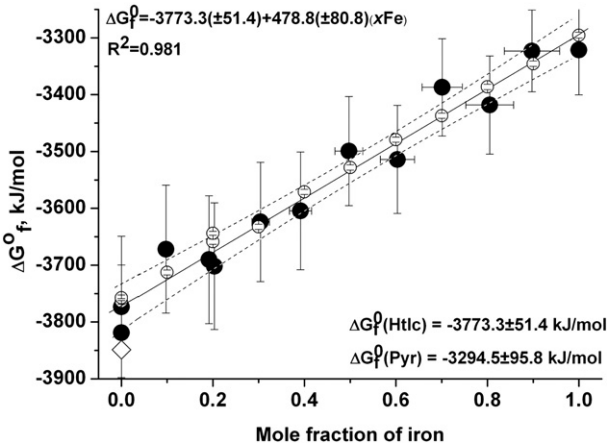

Fig. 9. Gibbs free energies of "water-free" solids calculated as a function of the mole fraction of iron. Filled symbols are calculated including uncertainties of stoichiometric coefficients (see text above). Open symbols are calculated including only uncertainties of concentrations of relevant dissolved components (Mg, Al ± 50%, Fe ± 66%) and using idealized stoichiometric coefficients $Mg_3Al_{1-x}Fe_x(OH)_8(CO3)_{0.5}$. The diamond symbol represents a result from Allada et. al [2005], converted to water-free conditions and normalized to Mg_3-stoichiometry. Dashed lines indicate the 95% confidence interval.

Converting this value to the "water-free" basis and normalizing the stoichiometry to three Mg (i.e., $Mg_3Al_{1.054}(OH)_{8.108}(CO_3)_{0.527}$) gives -3853.8 ± 8.4 kJ/mol.

4. Conclusions and discussion

Hydrotalcite–pyroaurite samples containing different mole fractions of Fe were successfully synthesized by a co-precipitation method at ambient conditions (23 ± 2 °C, 1 bar) and constant pH $\approx 11.40 \pm 0.03$. The $Mg^{2+}/(Al^{3+} + Fe^{3+})$ ratios of the precipitated solids were kept constant at 2.91 ± 0.15; only the Fe^{3+}/Al^{3+} ratio was varied between 0 and 1.

All PXRD patterns indicate the formation of a single phase belonging to the hydrotalcite–pyroaurite solid-solution series [6,7]. A clear linear relationship was observed between the lattice parameter a_o (equal to 3.060 ± 0.001 for hydrotalcite and 3.110 ± 0.001 Å for pyroaurite) and the mole fraction of iron, in agreement with Vegard's law, thereby confirming the existence of a solid solution. The variation observed for the c_0 parameter is quite small but higher than the uncertainty, so the trend seems correct. From the available data it is difficult to distinguish variations caused by longer M–OH distances from those caused by interlayer water content.

The thermal behavior is that expected for LDH with 3 main decomposition steps. These 3 events are delayed when the iron content is decreased, reflecting some strengthening of binding forces at high mole fractions of Al. This is consistent with the fact that Fe–OH distances are longer than Al–OH distances. TGA measurements were used here successfully for measuring the water- and carbonate content of the precipitated solids. For hydrotalcite-like phases this is usually difficult to achieve because the three different decomposition steps are often not well separated.

The low stability of iron-rich samples under laser irradiation precludes a complete characterization of the solid-solution series by laser-Raman spectroscopy. The typical peaks around 540 cm^{-1} result from the interaction of H_2O with the carbonate in the interlayers. Unfortunately the Raman bands disappear in the whole wavenumber region from 250 to 3800 cm^{-1} when the mole fraction of iron exceeds about 0.5. As mentioned above, TGA experiments reveal that iron-rich compositions are less stable with respect to temperature. Similarly, de Faria et al. [17] showed that the energy deposited by the laser beam leads to disappearance of bands in the magnetite–hematite system. Since we used beam powers of around 40 mW on the sample as well as long acquisition times in our own measurements, we cannot rule out similar effects of thermal decomposition during recording of the spectra.

As outlined in the introduction, an extended aim of the present study included quantifying the Gibbs free energies of members of the solid-solution series. This can be achieved by measuring solution- and solid components under the assumption that thermodynamic equilibrium between precipitated solid and mother solution was reached. All these analyses were performed and the results are illustrated in Fig. 9. It turned out that the precision obtained is not yet satisfactory for applications of the data to problems of waste management. The uncertainties of the estimated Gibbs free energies, for example for the two end-members hydrotalcite and pyroaurite, lie between 50 and 100 kJ/mol. Converted into the usually used $\log_{10}$-units this corresponds to uncertainties of 10 to 20 orders of magnitude in solubility. A quick analysis shows that these large uncertainties arise from uncertainties in the analyses of the solid phases (see Table 3). Uncertainties in composition of the solutions, although substantial from the point of view of absolute values, are much less significant with respect to the total uncertainties.

There is, however, another point that should be taken into account. The present Gibbs free energy analysis started from the assumption that the system can be described using a simple and ideal binary solid-solution model with the two end-members hydrotalcite and pyroaurite. Most likely, this view is too simplistic. From ongoing investigations on C–S–H systems there are strong indications that enhanced solid-solution models (e.g. [18]) may better describe the hydrotalcite–pyroaurite system. Work on this topic is ongoing.

To conclude, we clearly see the need to perform more precise analytical work and to reverse the experiments. Solubility experiments on hydrotalcite–pyroaurite solid solutions including iron-55 tracers have therefore been started. The results of combining these modified approaches will be the subject of a forthcoming publication.

Acknowledgements

We wish to thank Dr. U. Eggenberger, M. Eggimann, C. Wanner — for their help with PXRD analyses; M. Fisch, M. Painsi — for their support with Raman spectroscopy; Dr. Th. Arlt — support with TGA measurements; and for financial support the Nationale Genossenschaft für die Lagerung radioaktiver Abfälle (NAGRA).

References

[1] F. Cavani, F. Trifiro, A. Vaccari, Hydrotalcite-type anionic clays: preparation, properties and applications, Catalysis Today 11 (1991) 173–301.
[2] A. de Roy, C. Forano, M. EL Malki, J.-P. Besse, Anionic clays: trends in pillaring chemistry, in: M.L. Occelli, H.E. Robson (Eds.), Synthesis of Microporous Materials, Expanded Clays and Other Microporous Solids, Van Nostrand Reinhold, New York, 1992, p. 108.
[3] J. Rodriguez-Carvajal, FULLPROF: A Program for Rietveld Refinement and Pattern Matching Analysis, Abstracts of the Satellite Meeting on Powder Diffraction of the XV Congress of the IUCr, Toulouse, France, 1990, p. 127.
[4] Research package for thermodynamic modelling of aquatic (geo)chemical systems by Gibbs Energy Minimization, http://gems.web.psi.ch.
[5] Wolfgang Hummel, U. Berner, Enzo Curti, F.J. Pearson, Tres Thoenen, Nagra/PSI Chemical Thermodynamic Data Base 01/01, Universal Publisher/uOublish.com, Parkland, Florida, 2002.
[6] H.C.B. Hansen, C.B. Koch, Synthesis and characterization of pyroaurite, Applied Clay Science 10 (1–2) (August 1995) 5–19 (Synthesis and Application of Anionic Clays).
[7] G.J. Ross, H. Kodama, Properties of a synthetic magnesium–aluminum carbonate hydroxide and its relationship to magnesium–aluminum double hydroxide, manasseite and hydrotalcite, American Mineralogist 52 (1968) 1036–1047.
[8] A.R. Danton, Ashcroft, Vegard's law, Physical Review 43 (6) (1991) 3161–3164.
[9] R.D. Shannon, Revised effective ionic-radii and systematic studies of interatomic distances in halides and chalcogenides, Acta Crystallographica Section A 32 (1976) 751–767.
[10] M. Bellotto, B. Rebours, O. Clause, J. Lynch, D. Bazin, E. Elkaïm, A reexamination of hydrotalcite crystal chemistry, Journal of Physical Chemistry 100 (1996) 8527–8534.
[11] S. Miyata, Physicochemical properties of synthetic hydrotalcites in relation to composition, Clays and Clay Minerals 28 (1980) 50–56.
[12] V. Vagvolgyi, S.J. Palmer, J. Kristof, R.L. Frost, E. Horvath, Mechanism for hydrotalcite decomposition: a controlled rate thermal analysis study, Journal of Colloid and Interface Science 318 (2008) 302–308.
[13] V. Rives, Characterisation of layered double hydroxides and their decomposition products, Materials Chemistry and Physics 75 (2002) 19–25.
[14] R.L. Frost, B.J. Reddy, Thermo-Raman spectroscopic study of the natural layered double hydroxide manasseite, Spectrochimica Acta. Part A: Molecular and Biomolecular Spectroscopy 65 (2006) 553–559.
[15] National Water Quality Laboratory, Technical Memorandum 94-08, http://nwql.usgs.gov/Public/tech_memos/mwql.94-08.html.
[16] R.K. Allada, A. Navrotsky, J. Boerio-Goates, Thermochemistry of hydrotalcite-like phases in the MgO–Al_2O_3–CO_2–H_2O system: a determination of enthalpy, entropy, and free energy, American Mineralogist 90 (2005) 329–335.
[17] D.L.A. Faria, S. Venâncio Silvia, M.T. de Oliveira, Raman microspectroscopy of some iron oxyhydroxides, Journal of Raman spectroscopy 28 (1997) 873–878.
[18] J. Bruno, D. Bosbach, D. Kulik, A. Navrotsky, Chemical thermodynamics of solid solutions of interest in radioactive waste management: a state-of-the art report, in: F.J. Mompean, M. Illemassene, J. Perrone (Eds.), Chemical Thermodynamics Series, vol. 10, OECD, Paris, 2007, pp. 6–100.